

A Comparison of Texture Development in an Experimental and Industrial Tertiary Oxide Scale in a Hot Strip Mill



XIANGLONG YU, ZHENGYI JIANG, JINGWEI ZHAO, DONGBIN WEI, JI ZHOU, CUNLONG ZHOU, and QINGXUE HUANG

Electron backscatter diffraction (EBSD) has been used to investigate the microstructure and texture-based features of an industrial tertiary oxide scale formed on a micro-alloyed low-carbon steel from a hot strip mill. EBSD-derived maps demonstrate that the oxide scale consists primarily of magnetite (Fe_3O_4) with a small amount of hematite ($\alpha\text{-Fe}_2\text{O}_3$) which scatters near the surface, at the oxide/steel interface and at the cracking edges. The results extracted from these maps reveal that there is a significant difference between the industrial and the laboratory oxide scales in their grain boundaries, phase boundaries, and texture evolutions. There are high proportions of special coincidence site lattice boundaries $\Sigma 3$ and $\Sigma 13\text{b}$ in the magnetite of the industrial oxide scale, rather than the lower orders of $\Sigma 5$, $\Sigma 7$, and $\Sigma 17\text{b}$, which develop in the experimental oxide scale. Within the phase boundaries, the orientation relationships between the magnetite and the hematite correspond to the matching planes and directions $\{111\}\text{Fe}_3\text{O}_4\|\{0001\}\alpha\text{-Fe}_2\text{O}_3$ and $\{110\}\text{Fe}_3\text{O}_4\|\{110\}\alpha\text{-Fe}_2\text{O}_3$. Magnetite in both of these oxide scales develops a relatively weak $\{001\}$ fiber texture component including a strong $\{001\}\langle 100 \rangle$ cube and a slightly strong $\{100\}\langle 210 \rangle$ texture components. Unlike the $\{001\}\langle 110 \rangle$ rotated cube component in the experimental oxide scale, the magnetite in the industrial tertiary oxide scale develops a strong $\{112\}\langle 110 \rangle$ and a relatively strong $\{113\}\langle 110 \rangle$ and $\{111\}\langle 110 \rangle$ texture components. These findings have the potential to provide a convincing step forward for oxidation research.

DOI: 10.1007/s11663-015-0443-6

© The Minerals, Metals & Materials Society and ASM International 2015

I. INTRODUCTION

MICRO-ALLOYED low-carbon steel is a typical low-carbon composite alloy generally with a micro-amount of Nb, V, and Ti additions, either individually or together, in order to achieve mechanical properties

that low-carbon steel on its own does not have. These mechanical properties include high strength while still maintaining adequate toughness, weldability, ductility, and formability.^[1-3] Because of this, the as-hot-rolled micro-alloyed steel without subsequent processing such as cold rolling has the potential to become an ideal candidate for a wide range of promising applications, particularly in automotive applications for fuel efficiency and weight saving.^[4] Another promising potential for the Nb-V-Ti micro-alloyed steel lies in the tight oxide scale formed on the surface of the hot-rolled strip due to thermal oxidation at elevated temperatures.^[5,6] Along with the steel substrate, the tight oxide scale is expected to deform without blistering failures and to further enhance the tribological properties of the as-hot-rolled steels during the downstream metal forming process.^[7-9] This means that we need to further characterize the microstructural and crystallographic features of the oxide scale formed on the hot-coiled steel after coiling during hot rolling,^[10,11] *i.e.*, the tertiary oxide scale.

The oxide scale formed in the particular case of hot rolling can generally be classified as the primary, secondary, and tertiary oxide scales, normally corresponding to the reheating stages, roughing stages, and finishing passes of continuous mills, respectively.^[7,12] The tertiary oxide scale grows during the finishing rolling and the subsequent cooling down to the ambient temperature, as it is also deformed while the steel is

XIANGLONG YU, Postdoc, formerly with School of Mechanical, Materials and Mechatronic Engineering, University of Wollongong, Wollongong, NSW 2522, Australia, is now with the School of Materials Science and Engineering, Tsinghua University, Beijing 100084, China. ZHENGYI JIANG, Professor, is with the School of Mechanical, Materials and Mechatronic Engineering, University of Wollongong, and also with the Shanxi Provincial Key Laboratory on Metallurgical Device Design and Theory, Taiyuan University of Science and Technology. JINGWEI ZHAO, Research Fellow, is with the School of Mechanical, Materials and Mechatronic Engineering, University of Wollongong. DONGBIN WEI, Senior Lecturer, is with the School of Mechanical, Materials and Mechatronic Engineering, University of Wollongong, and also with the School of Electrical, Mechanical and Mechatronic Systems, University of Technology, Sydney, NSW 2007, Australia. JI ZHOU, Professor, is with the School of Materials Science and Engineering, Tsinghua University. QINGXUE HUANG, Professor, is with the Shanxi Provincial Key Laboratory on Metallurgical Device Design and Theory, Taiyuan University of Science and Technology. Contact emails: jiang@uow.edu.au, zcunlong@163.com

Manuscript submitted March 29, 2015.

Article published online August 25, 2015.

processed.^[13,14] This layer of oxide scale may evolve further and undergo structural changes if oxygen is available during air cooling after coiling.^[15,16] Like most engineering alloys, the tertiary oxide scale has a complex microstructure, with microstructural heterogeneities such as inhomogeneously distributed precipitates, a distribution of grain size and microtextures, and varying grain boundary characteristics.^[17,18] Generally, the tertiary oxide scale consists of a thin outer layer of hematite (α -Fe₂O₃), an intermediate layer of magnetite (Fe₃O₄), and an inner layer of wustite (Fe_{1-x}O, with $1 - x$ ranging from 0.83 to 0.95) just above the steel substrate.^[12,19] The distribution of these oxide phases depends largely on the heat treatment and atmospheric conditions during hot rolling and the alloying elements in the steel composition.^[20,21] The changes that take place in wustite decomposition below 843 K (570 °C) or the transformation of magnetite to hematite become fundamental and of great practical interest if we wish to make an easy and controllable oxide microstructure available.^[22,23] Little research has been done on the characterization of crystallographic texture evolution in tertiary oxide scale.

With the advance of electron backscatter diffraction (EBSD), it has shown the potential to aid in the understanding of the crystallographic aspects of microstructures and to be used in a wide variety of materials.^[24,25] Automated EBSD has shown a great potential for characterizing the spatial distribution of crystallographic orientation within a multiphase microstructure as well as for quantitative analysis of these phase transformations.^[26,27] Some studies^[28,29] on crystallographic texture in oxide scale are now being performed using EBSD. Spinel magnetite and cubic wustite share a strong $\langle 100 \rangle$ texture in undeformed oxide scale whatever the steel substrate.^[30-32] In contrast, the deformed oxide scale develops a pronounced $\{100\}$ fiber component using plane strain compression.^[33] Little is currently known concerning the grain boundary characteristics and the crystallographic texture of magnetite in the industrial oxide scale formed on hot-coiled strips after coiling.^[34]

The present work brings us closer to the industrial site to identify the microstructure, grain boundary characteristics, and texture development in the industrial oxide scale formed on a commercial hot-coiled steel strip after coiling during the hot rolling process, with particular emphasis on the difference between the tertiary oxide

scale produced in the industry and that produced in the laboratory.

A. Experimental and Analytical Procedures

The material used in this study is a commercial Nb-V-Ti micro-alloyed low-carbon steel for an automotive beam. Its chemical composition is listed in Table I. The steel strips were collected from an industrial hot-rolled coil with a finish-rolling temperature of 1133 K (860 °C) and a coiling temperature of 863 K (590 °C), as summarized in Table II.

As seen in Figure 1, the samples were taken from the middle coil along the middle length of the hot-rolled steel strip. This is because the coiling process introduces an asymmetry between the top and the bottom and between the middle and the edge of the steel strip. The former top surface of the steel sheet is generally pulled in tension during coiling, whereas the former bottom surface of the steel sheet is loaded in compression. The effect of load can differ in the location of the hot-coiled steel strip,^[35] depending on the surfaces. To avoid these effects, the upper surface of a steel strip is used in this study. Unlike the industrial oxide scale, the experimental oxide scale was obtained by one-pass hot rolling with a thickness reduction of 28 pct at 1133 K (860 °C), followed by a cooling rate of 28 K/s.^[36]

In order to fit into the sample holder of the ion milling stage, the samples were sectioned into blocks of dimensions $20 \times 20 \times 7.8 \text{ mm}^3$ using a Struers Accutum-50 cutting machine. The samples are taken from the center of the hot-rolled sheets along the planes perpendicular to the rolling direction (RD) and parallel to the oxide growth. Because of this, the sample surface of the oxide scale was oriented toward the normal direction (ND). The gage length and width of the rolling

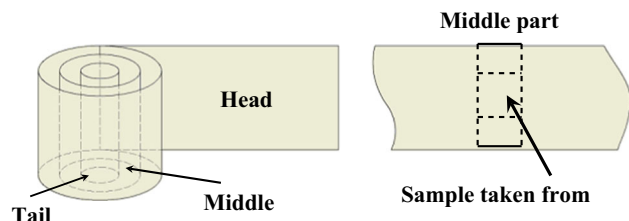


Fig. 1—Scheme of the locations of the samples in the hot-rolled steel strip.

Table I. Chemical Compositions of the Studied Steel

Elements	C	Si	Mn	P	Cr	S	Al	N	Nb + V + Ti	Fe
Weight percent	0.1	0.15	1.61	0.014	0.21	0.002	0.034	0.003	0.016-0.041	bal.

Table II. Processing Parameters of the Studied Steel in Commercial Hot Rolling

Temperature	Reheating	Roughing (RT2)	Finishing (FT6)	Coiling (CT)
K (°C)	1523 K (1250 °C)	1333 K (1060 °C)	1133 K (860 °C)	863 K (590 °C)

sample were parallel to the RD and traverse direction (TD) of the hot-rolled strip, respectively. After cutting the sample, one of the broad faces on the sample was ground to a surface finish of $0.6\ \mu\text{m}$ using SiC papers of 800, 1200, 2400, and 4000 mesh. Prior to ion milling, the samples were cleaned in ethanol using ultrasonic agitation and then stored in a desiccator.

Sample preparation for subsequent cross-sectional examination with an electron microscope was performed on a Leica EM triple ion beam cutter (TIC020) system. After gold deposition on one polished edge, the samples were then ion-milled at 6 kV for 5 hours of precise processing. When taken from the mask of the ion miller, samples were ready for EBSD. As magnetite and hematite do not present charging problem in the electron microscopes, carbon coating was unnecessary. In the case of ion milling at 6 kV, such high-energy ion beam may modify the surface due to the momentum and induced heating. Hence, a variable sample turning velocity was used during ion milling to alleviate the influence of sample preparation on the electron microscopy and EBSD mapping. The surface modification due to induced heating during ion milling may have an influence on multiphase materials.^[37,38] Nevertheless, such an influence on required datasets can be alleviated by a combined EBSD—energy dispersive spectroscopy (EDS) analysis.^[30,36]

Microstructural characterization was studied using a JEOL JSM 7001F Schottky field emission gun (FEG) scanning electron microscope (SEM) with a Nordlys-II (S) EBSD detector. The samples that etched with 2 pct nital solution for 20 seconds were characterized by SEM under SEM-secondary electron imaging (SEI) and SEM-backscattered electron (BSE) modes. The EBSD dataset was acquired and indexed using the Channel 5 software package. Preferred orientation measurements of the oxide scale were done *via* automatic beam scanning, with a step size of 8 nm on a predefined area of $12 \times 8\ \mu\text{m}$. The main setup parameters used in the present study were a tilt angle of 70 deg, a working distance of 15 mm, an acceleration voltage of 15 kV, a probe current of around 2–5 nA, and a mean angular deviation (MAD) for data acquisition of 2 deg. The minimum and maximum numbers of detected bands were 4 and 5, respectively.

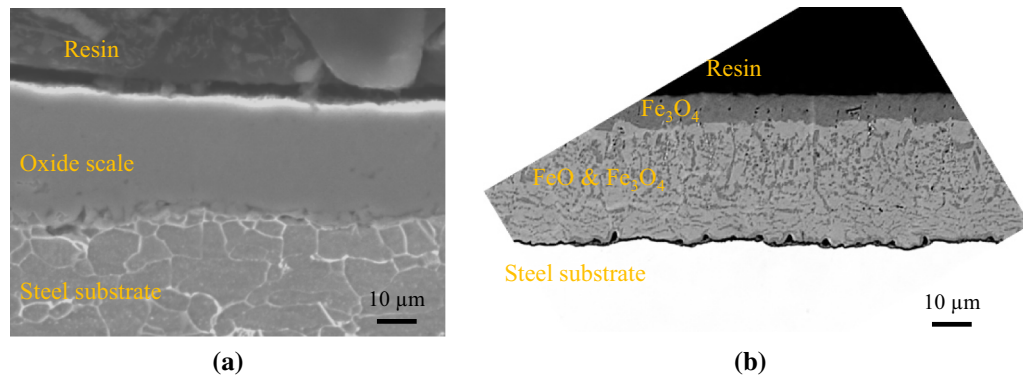


Fig. 2—(a) SEM-SEI image of the sample for the industrial tertiary oxide scale and (b) SEM-BSE images of the sample for experimental oxide scale before hot rolling.

Post-processing of the resulting dataset was carried out using Channel 5 software, where both orientation mapping and texture data were extracted from the EBSD maps. After the noise reduction, an angular resolution for the grain reconstruction was maintained at a constant value of 2 deg. Accordingly, $2\ \text{deg} \leq \theta < 15\ \text{deg}$ misorientations are defined as low-angle grain boundaries (LAGBs), whereas the high-angle grain boundaries (HAGBs) are $\theta \geq 15\ \text{deg}$. The orientation distributions of the oxide phases were calculated from the collected data on the individual grain orientations. The grain orientation $g = (\phi_1, \Phi, \phi_2)$ is expressed by the three Euler angles in Bunge notation.^[39] The probability density function of orientations g can be represented by the orientation distribution functions (ODF) in the form of sections through the orientation space. The ODF sections were calculated using the discrete binning method with a bin size of 5 deg and Gaussian smoothing. Our previous study^[36] also showed other details of the analytical procedures for such a multiphase oxide scale.

II. RESULTS AND DISCUSSION

A. Oxide Scale Distinction

Prior to the EBSD investigation, the oxide scale distinction was carried out by SEM under both SEM-SEI and SEM-BSE modes, as shown in Figure 2. It can be seen that the microstructure of the fine-grained polygonal ferrite and pearlite of the steel substrate when using SEM-SEI (Figure 2(a)) and a two-layer oxide scale composed of a thin outer magnetite layer and a thick eutectoid inner layer when using SEM-BSE (Figure 2(b)) can be clearly distinguished.

B. Grain Reconstruction and Phase Identification

This section and the corresponding figures are organized based on the analytical sequence of grain reconstruction using orientation microscopy. After indexing the diffraction pattern, each sampling point is stored with its phase identity, orientation, spatial coordinates, measure of fit or confidence index, and diffraction

pattern quality metric.^[26] The types of orientation mapping output depend on the information that is being sought, and many examples of varying complexity are available.^[25,26,32] In this study, the multiphase oxide scale is composed of cubic wustite, spinel magnetite, trigonal hematite, and bcc steel substrate. Some of the representative EBSD-derived maps are shown in Figures 3 and 4 in an order of band contrast (BC), phase, and grain boundary maps of the industrial and experimental oxide scales, respectively. First, the pattern quality index may be different for different phases in a sample, and this can sometimes be exploited in order to distinguish phases which have the same crystal structure. In this study, the BC maps serve as preliminary phase identification and evaluation of the indexing. Second,

phase maps are given followed by grain boundary maps. For clarity, the three types of maps have been constructed individually in standard form^[26,32] in order to avoid overlaps of various maps.

The pattern quality map, *e.g.*, BC map in Figure 3(a), is generally grayscale which appears similar to coarse SEM images, in part because every point on the map is assigned a gray value based on the pattern quality for that point.^[24,26] Here the BC map of the industrial oxide scale in Figure 3(a) is darker than that of the experimental tertiary oxide scale in Figure 4(a). Grain boundaries are normally darker because there are low-pattern quality linear features and the image is highly sensitive to orientation. In addition to grain boundaries, some areas near the surface and/or near cracks appear darker in the BC maps because of the degradation of the pattern quality. This low image quality is attributed to a combined pattern, where the diffraction volume has crystal lattices in different orientations when the beam is located at a boundary. There are a number of other factors which can also affect the image quality. When the dark areas appear in the multiphase oxide scale, phase identification becomes necessary.

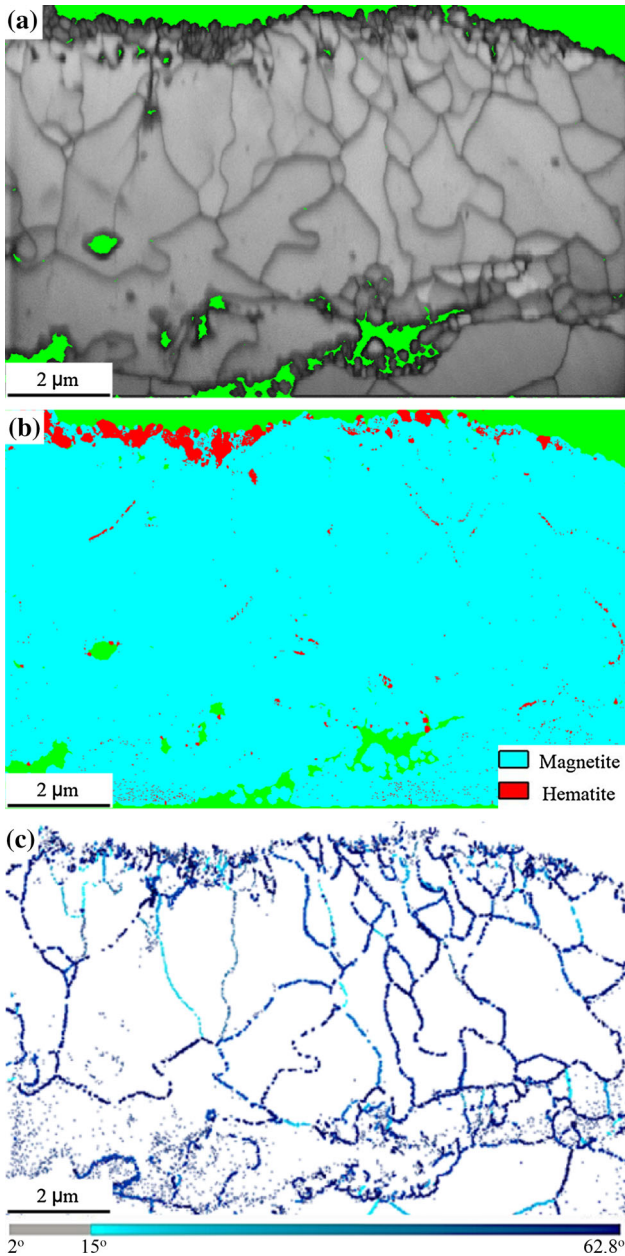


Fig. 3—EBSD (a) band contrast (BC), (b) phase, and (c) grain boundary maps of the industrial tertiary oxide scale.

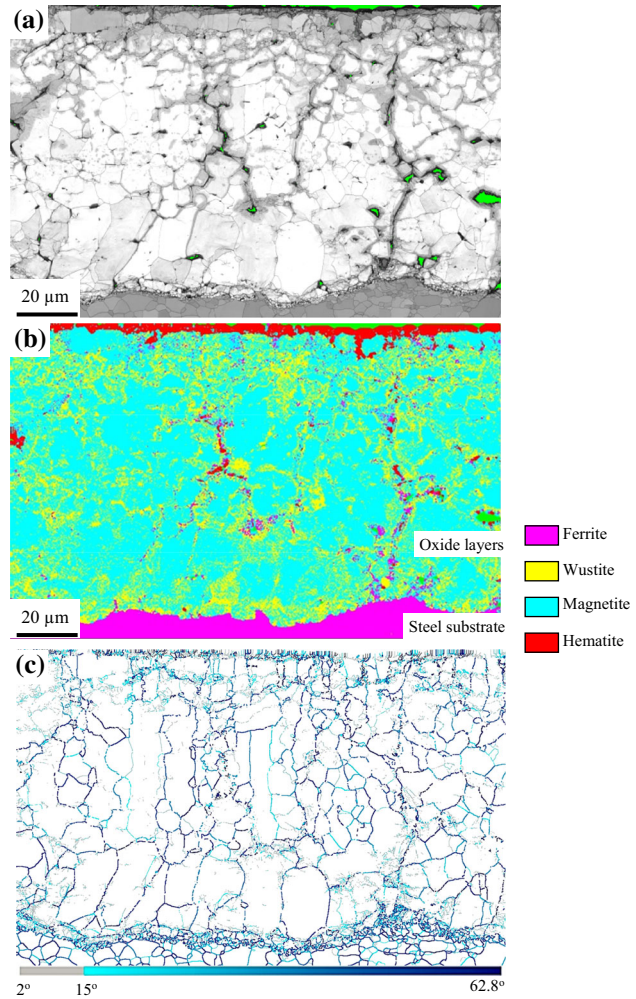


Fig. 4—EBSD (a) band contrast (BC), (b) phase, and (c) grain boundary maps of the experimental tertiary oxide scale.

Figure 3(b) presents a representative EBSD phase map of the industrial oxide scale, where magnetite and hematite are colored cyan and red, respectively. The oxide scale consists of a two-layered microstructure with a relatively thin outer layer of hematite and an inner magnetite layer. Hematite near the surface gradually penetrates into the cracks within the oxide scale, sometimes scattering over the magnetite matrix. This can also be seen in the experimental tertiary oxide scale in Figure 4(b). Since the grain size of the hematite seen here is very small, in particular at the magnetite grain boundaries, it is necessary that the calculated and observed hematite patterns be carefully matched. Based on previous studies,^[12,16] it was thought that the hematite is located in the two edges of the hot-coiled strip rather than in the inner layer of oxide scale. The growth of the hematite, however, takes place on both the oxygen/hematite interface (sustained by diffusion of iron through the hematite layer into the hematite/oxygen interface) and the magnetite/hematite interface (sustained by oxygen diffusion through the hematite layer).^[20,21] This means that it is likely that the oxidation of the magnetite to the hematite near the surface and near the cracks leads to a high fraction of local misorientation as their lattice misfits.^[18,32] This phenomenon can also be found in the ‘red scale’ (hematite) during high-temperature processing, especially when magnetite is oxidized and becomes red powdery hematite during subsequent air cooling.^[40,41] The amount of wustite is greater than that of hematite in the experimental tertiary oxide scale in Figure 4(b). This is because wustite is thermally unstable and will decompose into magnetite and ferrite below 843 K (570 °C).^[20,21] The dispersed wustite in the experimental tertiary oxide scale can be attributed to the fact that an oxidation reaction among iron oxides could occur to preserve the thermally grown wustite with granular grains during the cooling process.^[22,23]

The grain boundary map of the industrial oxide scale in Figure 3(c) illustrates the columnar boundary structure corresponding to Figure 3(a). Typically, grain boundaries with misorientations between 2 and 15 deg are considered as subgrain or low-angle grain boundaries and shown in silver color, whereas boundaries with misorientations higher than 15 deg are considered as random high-angle grain boundaries shown in blue shades based on the misorientation angle. Specification of the misorientation between neighboring grains provides access to the grain boundary crystallography by providing some information about the distribution of grain boundary geometry.^[26,42] In the grain boundary map of Figure 3(c), the different colors of the grain boundaries are varying over the scanning area. For example, the dark blue at the grain boundary indicates that the spatially connected grains show large variation in their crystallographic orientation due to the existence of plastic strain among these neighboring grains.^[43] Afterwards, the subsequent orientation maps show specific orientation changes at the interfaces and other aspects of interface crystallography. Combining BC map with the phase map, it can be seen that the globular grains appear in the surface layer and near the oxide/

steel interface. Despite this, the columnar morphology of the industrial oxide scale, as claimed by experimental studies in the laboratory (Figure 4(c)), is not obvious here (Figure 3). The difference between the central layer and the upper/lower layers in the industrial oxide scale is in grain size rather than in grain morphology. Unlike the interface layer of smaller grains near the steel substrate, as seen in Figure 4, the oxide–metal interface is not visible in Figure 3. This is caused, in part, because spallation to the industrial tertiary oxide scale can easily occur during sample preparation.

The resulting localized oxidation is related to local stress intensity such as oxide (or oxide and substrate) creep and grain orientation.^[28,44,45] If the stresses in an oxide scale become greater than that which can be accommodated by elastic strain, and if plastic deformation is insufficient to relieve the stress, mechanical disruption of the system, such as scale spallation, will occur.^[21,46,47] Spallation means the separation and ejection of fragments from the oxide scale.^[48] The underside of a separated scale will dissociate preferentially at oxide grain boundaries, where outward diffusion of metal is the fastest. This process can then create microchannels along favorably oriented boundaries, allowing subsequent inward transport of the molecular oxidant.^[20,21] The mechanical failure of oxide scales, which leads to their spallation, and the consequential acceleration in the rate of alloy failure greatly depend on its stress state, properties, and microstructure, which can change with temperature.^[46,48] In this case, the industrial oxide scale still adhered to the steel substrate during sample preparation and EBSD analysis, but there are large pores at the oxide/steel interface, as shown in Figure 3(a), compared with the experimental oxide scale, as shown in Figure 4(a). This can be attributed to a combined mechanism of stress relief and re-oxidation,^[28,44] but the texture-based features are affected only in the vicinity of some cracks at the oxide–scale interface. Alternatively, the morphology, topography, and diffraction pattern of an oxidizing substrate can be thermally imaged during *in situ* investigations.^[49–51] In any case, the adherence of oxide scale and steel substrate is a complex and important issue during oxidation process.^[21,52] The blistering or spalling failure depends on several factors, such as the thickness of oxide scale, heat treatment, alloying elements in the substrate, humid air or other atmospheres, *etc.* As seen in Figure 2, there are no blistering failures occurred in the oxide scale. This is possibly due to the high thickness of the oxide layer,^[8,52] and the alloying elements in the steel substrate.^[6] Nevertheless, it is probable that other failures, such as pores, can also serve as the microchannels for the re-oxidation, *i.e.*, wustite oxidizes to magnetite when contact with the steel substrate disappears. Indeed, different wustite decomposition behavior can result from a combined effect of different heat treatments and failures of the oxide scale.^[8,52]

C. Microstructural Characterization

The EBSD inverse pole figure (IPF) orientation map of the industrial oxide scale in Figure 5 identifies the

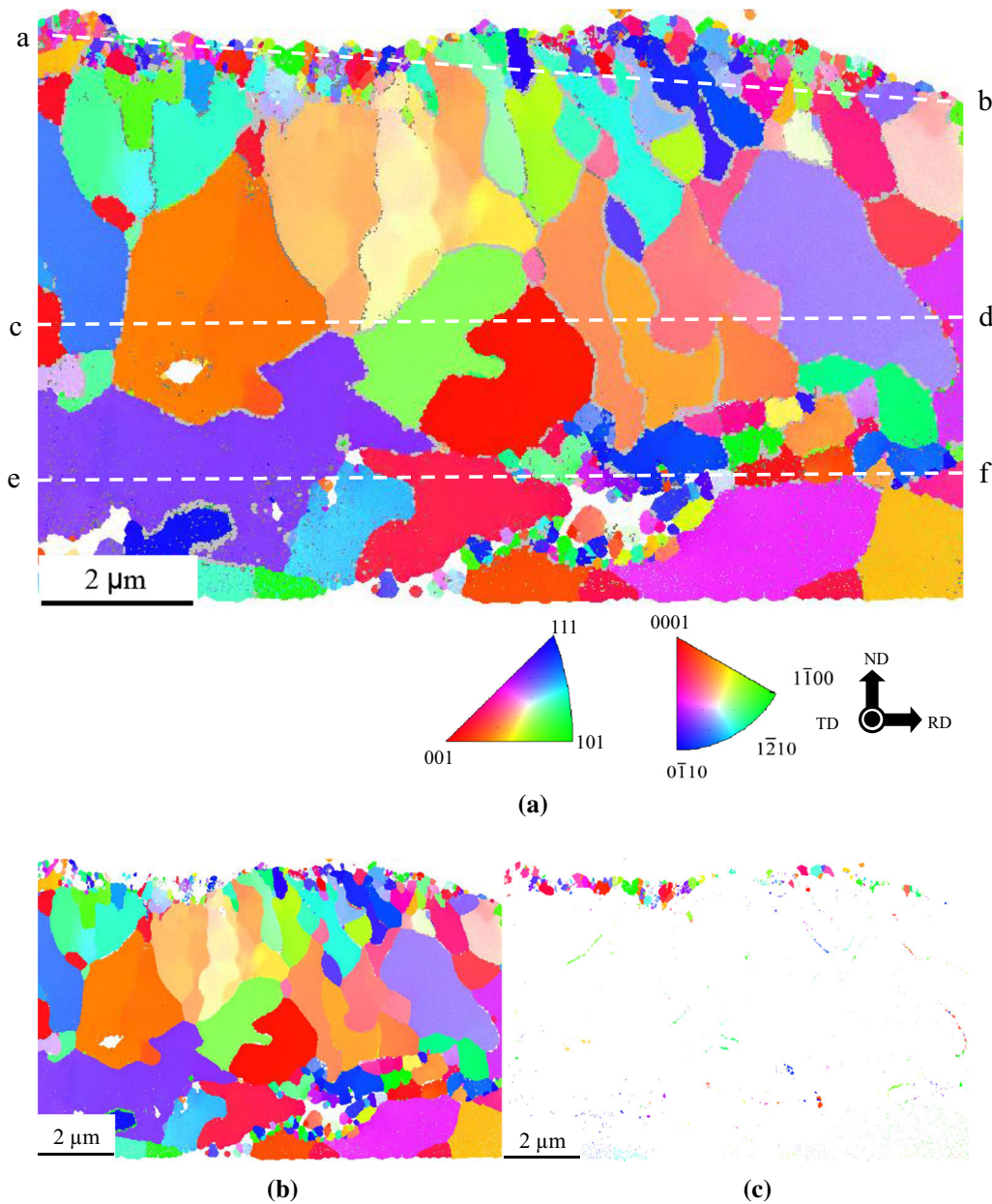


Fig. 5—(a) EBSD inverse pole figure (IPF) orientation map of the industrial tertiary oxide scale, the color keys showing for the cubic symmetry of magnetite and trigonal hematite. Lines a-b, c-d, and e-f lie along the outer-, intermediate- and inner-layer scales, respectively. The IPF subset for (b) magnetite and (c) hematite, separately.

orientation of grains using different colors. The color coded for the individual grains in the IPF map displays their absolute orientations in relation to a stereographical triangle. Different symmetry materials have different color keys, and the color keys are shown in Figure 5 for the cubic magnetite and trigonal hematite. In general, orientation microscopy refers to the automated measurement and storage of orientations according to a predefined pattern of coordinates on the sampling plane of the sample. The mapping of these orientations with reference to the sampling coordinates provides an orientation map of the spatial orientation distribution; that is, it derives the “orientation topography.”^[26,32] Color output is linked directly to the orientation and

accompanied by a key to the use of colors. This is often shown by assigning red, green, and blue to the 001, 011, and 111 corners, respectively, of the stereographic unit triangle for crystal directions that are parallel to a selected sample direction.^[26] This scheme works on all crystal systems except for that of triclinic symmetry. For example, the red colors shown in Figure 5 represent those points with the $\langle 100 \rangle$ parallel to the ND, *i.e.*, along the oxide growth direction. It should be noted that, as for an IPF, this representation displays only one direction of the 3D orientation information, and so rotations about this axis are not seen. This means that it is necessary for the orientation maps to combine all scanning maps (BC, phase map, and grain boundary

map), for a complete interpretation of the two phases of magnetite and hematite. It is noted that the color scheme of the legends in Figure 5 is a standard representation of stereographical triangle according to the crystal symmetry. Hence, it is difficult to distinguish the cubic magnetite and trigonal hematite, *i.e.*, with different symmetries, in one orientation (IPF) map of EBSD. For compromise during this stage, we have to set the two oxides, magnetite and hematite, into the two individual subsets, and therefore show their individual IPF, as shown in Figures 5(b) and (c).

As seen in Figure 5, most grains in the oxide scale have a relatively weak $\{001\}$ fiber texture component. This differs slightly from the orientation of the tertiary oxide scale after hot rolling. Before coiling of a steel strip, a strong $\{001\}$ fiber texture in the tertiary oxide scale was found.^[29,33] After coiling to hot-coiled strips, the weak intensity of this texture can contribute to the recovery and phase transformation of the oxide scale. Apart from the orientations, the IPF map can also demonstrate the microstructural features as observed in BC and grain boundary maps in Figure 3.

The local misorientation profile in Figure 6 shows the variation of grain boundaries in the outer, intermediate, and inner layers of the oxide scale, corresponding to lines a-b, c-d, and e-f, respectively, as shown in Figure 5(a). The distribution of misorientation angles in trigonal hematite (Figure 6(a)) has a cutoff at 95 deg, whereas cubic crystal magnetite (Figure 6(b) and (c)) has a maximum cutoff at 62.8 deg.^[26] There is a high fraction of grain boundaries in the outer (Figure 6(a)) and inner (Figure 6(c)) layers as the dense distributions in misorientation profiles. The distribution of misorientations was

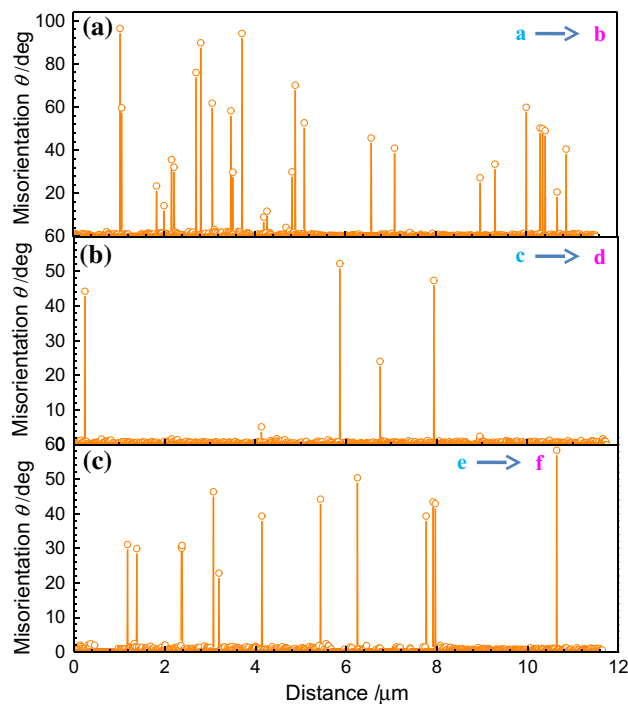


Fig. 6—Local misorientation distribution along the (a) outer-layer scale in the line a-b, (b) intermediate-layer scale in the line c-d, and (c) inner-layer scale in the line e-f, in Fig. 5.

inhomogeneous and differed grain by grain. In the present study, the intermediate layer has less misorientation in the same distance than the other two layers. This implies that the large grains are evidence of image analysis in Figures 3 and 5. This means that EBSD analysis can not only determine the complete orientation of grains, but it can also provide more information than the misorientation angle shown in the subsequent sections.

D. Grain Boundary Characteristics

EBSD is an essential tool in measuring the amount of coincidence site lattice (CSL) boundaries in oxide scale and the distribution of grain boundary characteristics. Figure 7 illustrates the histograms of overall CSL boundaries obtained for magnetite in the industrial and experimental oxide scales. The histogram contains the CSL boundaries of Σ -values less than 19. There is evidence that intergranular stress corrosion cracking has been shown to occur almost exclusively along random interfaces described by Σ -values greater than 29.^[53,54] The CSL boundary distributions shown in Figure 7(a) reveal that magnetite carries a high proportion of $\Sigma 3$ and $\Sigma 13b$, whereas the magnetite in the experimental oxide scale has a high proportion of $\Sigma 5$, $\Sigma 7$, and $\Sigma 17b$ (Figure 7(b)). It should be noted that coherent twins have been excluded from this analysis, thereby resulting in a significantly lower fraction of $\Sigma 3$ boundaries. The low- Σ CSL grain boundaries have been ascribed to the reduced free volume at the interfaces arising from the high degree of structural order.^[55,56] This means that certain particular types of boundaries are less susceptible to damage such as creep cavitation or corrosion than other boundaries with random interfaces that are characterized by higher-order Σ relationships.^[57,58] Previous studies^[59,60] reveal that intergranular corrosion in austenitic stainless steel can be significantly reduced by increasing the frequency of low-energy CSL boundaries. In particular, the special CSL boundary of $\Sigma 13b$ is much more crack resistant than those beyond $\Sigma 13b$ and the random high-angle boundaries.^[61] It becomes clear that these low CSL grain boundary characteristics in magnetite can be used to enhance crack resistance and to improve the integrity properties of oxide scale on the hot-rolled steel for constructing automotive beams.

The use of EBSD allows us to characterize the grain and phase boundaries with respect to their misorientation.^[62] An important observation obtained is the occurrence of crystallographic phase boundaries between the cubic magnetite and the trigonal hematite. Figure 8 shows the lattice correlation boundaries between magnetite (Mt) and hematite (Hm). This representative orientation relationship corresponds to the matching planes and directions $\{111\}_{Mt} \parallel \{0001\}_{Hm}$ and $\{110\}_{Mt} \parallel \{110\}_{Hm}$. The histogram of angle deviation in $\{111\}_{Mt} \parallel \{0001\}_{Hm}$ has a cutoff at 55 deg, whereas $\{110\}_{Mt} \parallel \{110\}_{Hm}$ has a maximum cutoff at 30 deg. These boundaries have settled down with the most frequent deviation angle below 5 deg, delimited by the dashed line in Figure 8. Two types of oxide scales share the similar trends, although the high proportion of the boundaries $\{110\}_{Mt} \parallel \{110\}_{Hm}$ appear at

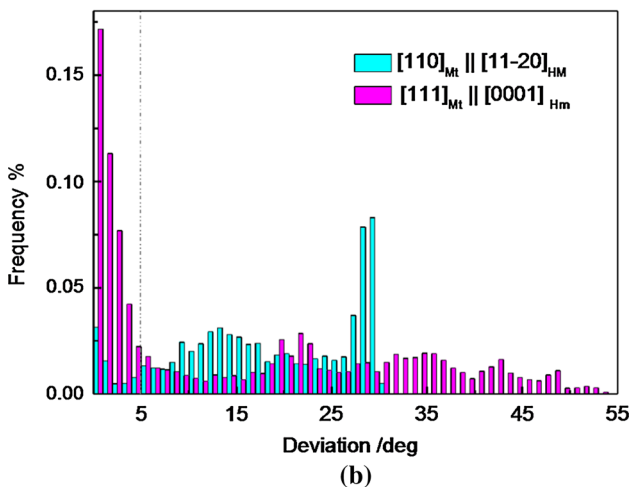
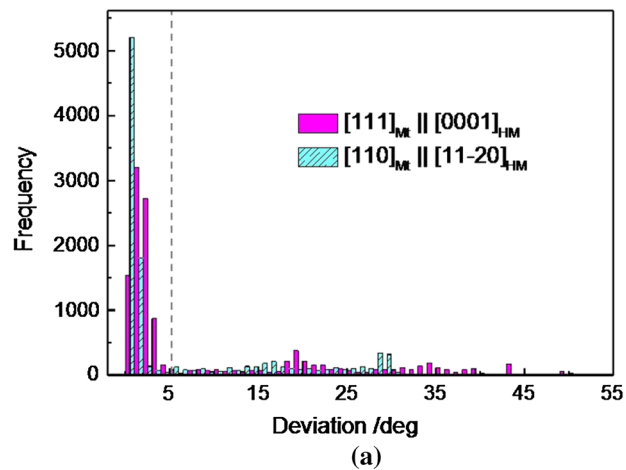
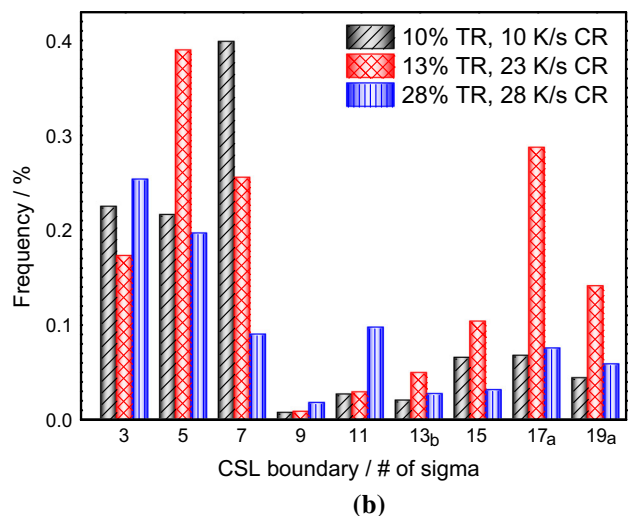
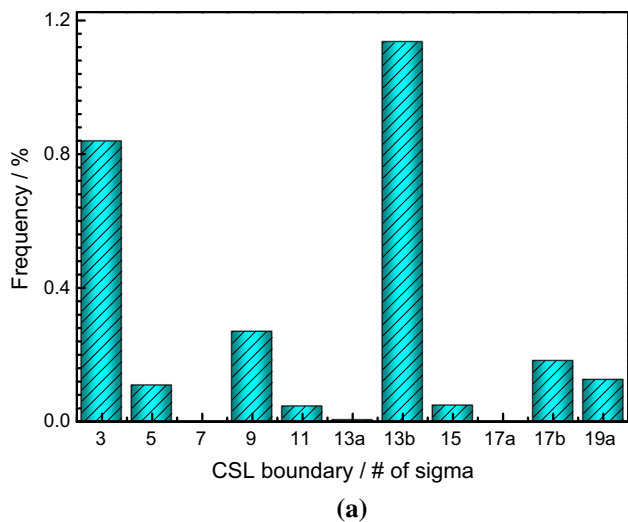


Fig. 8—Histogram of the lattice correlation boundaries between [111] of magnetite and [0001] of hematite, and [110] of magnetite and [110] of hematite, in the (a) industrial and (b) experimental tertiary oxide scales.

Fig. 7—Histogram plots of CSL boundary distribution for magnetite in the (a) industrial and (b) experimental tertiary oxide scales.

less than 30 deg (Figure 8(b)). The results show that the orientation of the basal planes of hematite coincides with the orientation of the octahedral planes of the magnetite. In most cases, the orientation relationship with low-angle boundaries suggests that the growth of new hematite grains occurs in the vicinity of the grain boundaries in the magnetite grains.

E. Texture Developments

The EBSD orientation dataset allows a detailed, microstructure-based analysis of texture. Figures 9 through 11 show the development of the crystallographic texture of the magnetite in industrial and experimental tertiary oxide scales and its intensity distributions along associated fibers or texture components. Figure 9 and Table III show schematically the ideal fibers in cubic materials and ODF distribution positions for selected sections of fixed ϕ_2 angles. In most cases, the relevant texture fibers for cubic materials are α , γ , and ϵ fibers lying on $\phi_2 = 45$ deg section at $\phi_1 = 0$, $\Phi = 55$ deg,

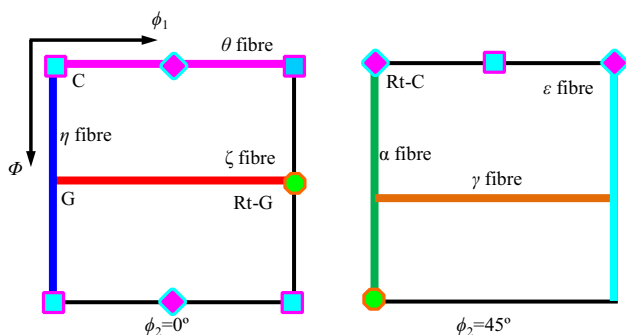
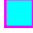





Fig. 9—Schematic representation of the position of the ideal fibers and cube texture component in cubic materials in the $\phi_2 = 0$ and 45 deg ODF sections.^[10]

and $\phi_1 = 90$ deg, corresponding to crystallographic fiber axis around $\langle 110 \rangle // RD$, $\langle 111 \rangle // ND$, and $\langle 011 \rangle // TD$, respectively, and η , θ , and ζ fibers superimposed on $\phi_2 = 0$ deg section at $\phi_1 = 0$, $\Phi = 0^\circ$, and $\Phi = 45$ deg, with the rotations of $\langle 100 \rangle // RD$, $\langle 100 \rangle // ND$, and $\langle 110 \rangle // ND$, respectively.^[33]

Table III. Euler Angles and Miller Indices for Some Common Texture Components in Cubic Metals and Alloys

Texture Component	Symbol	Euler Angles (deg)			Miller Indices	Fiber
		ϕ_1	Φ	ϕ_2		
Cube (C)		45	0	45	$\{001\}\langle 100 \rangle$	$\langle 100 \rangle$
Goss (G)		90	90	45	$\{110\}\langle 001 \rangle$	$\langle 100 \rangle$
Rotated goss (Rt-G)		0	90	45	$\{011\}\langle 011 \rangle$	$\langle 110 \rangle$
Rotated cube (Rt-C)		0/90	0	45	$\{001\}\langle 110 \rangle$	$\langle 110 \rangle$

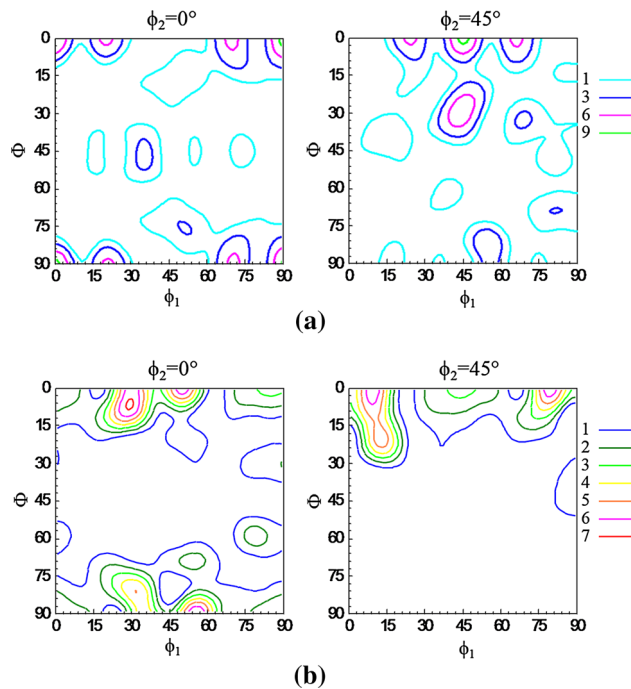


Fig. 10—Texture development in ODF $\phi_2 = 0$ and 45 deg sections of magnetite in the (a) industrial and (b) experimental tertiary oxide scales.

Magnetite has a cubic structure, and its ODF sections are depicted using the $\phi_2 = 0$ and 45 deg (Figure 10) in terms of the Bunge system. As seen in Figure 10(a), magnetite contains a strong $\{001\}\langle 100 \rangle$ cube texture component with a maximum intensity $f(g)$ up to 10 (Figure 11(a)). A relatively weak θ fiber develops in magnetite (Figure 10) superimposed on the $\phi_2 = 0$ deg section at $\Phi = 0$ deg with rotations of $\langle 100 \rangle // \text{ND}$. This fiber extends from the cube component to the pronounced $\{001\}\langle 210 \rangle$ orientations along $\phi_1 = 0-90$ deg. In particular, it can be seen that the location of the texture component in industrial oxide scale is much closer to $\{001\}\langle 210 \rangle$ than that in experimental tertiary oxide scale (Figure 11(a)). The relatively strong $\{100\}\langle 210 \rangle$ component records a second maximum texture intensity $f(g) = 6.7$. The value of the intensity here from the industrial production lines is the same as the experimental tertiary oxide scale. This texture development has also been found in previous studies^[28,33] using plane strain compression tests. The

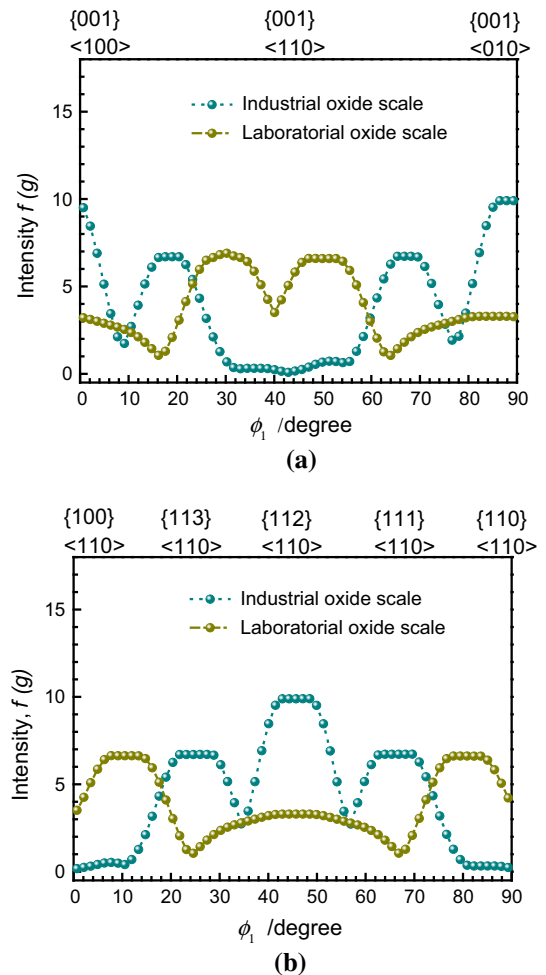


Fig. 11—Development of texture intensity $f(g)$ along the (a) θ and (b) $\langle 110 \rangle$ fibers of magnetite in the industrial and experimental tertiary oxide scale.

difference, however, is the absence of the $\{001\}\langle 110 \rangle$ rotated cube component, due partly to shifting from $\{113\}\langle 110 \rangle$ and $\{111\}\langle 110 \rangle$ to $\{112\}\langle 110 \rangle$, as shown in Figure 11(b). This can be ascribed to the recovery and recrystallisation in oxide scale on hot-coiled strips after coiling. A similar case can be seen in the IPF maps of oxide scale in Figure 3.

Comparing hot-rolled automotive parts with laboratory samples, the microstructure and texture development demonstrate that the difference between them is

due in part to their different heat treatments and processing, ranging from hot rolling, accelerated cooling to coiling. The results of this study show that much research still needs to be done. One area to be studied concerns what happens to the industrial oxide scale between controlled cooling on the run-out table and its final room-temperature state. In the present work, we have limited our study to the difference between the final oxide scale from the industrial products and those made in the laboratory.

III. CONCLUSION

An investigation into the overall microstructure and texture development in an industrial tertiary oxide scale from a hot strip mill has been systematically carried out using EBSD. The findings in the present work have been compared quantitatively with those of the experimental tertiary oxide scale. The following conclusions can be drawn:

1. The industrial oxide scale consists of a two-layered microstructure with a relatively thin outer layer of hematite and an inner magnetite layer. Its EBSD-derived BC map is darker than that of the experimental tertiary oxide scale, and this is due partly to the penetration of hematite into magnetite along the crack edges within the oxide scale.
2. The columnar morphology and the oxide-metal interface in the industrial oxide scale are not obvious from the EBSD map because of easy spallation of oxide scale during sample preparation.
3. Special CSL grain boundaries in magnetite of industrial oxide scale develop a high proportion of $\Sigma 3$ and $\Sigma 13b$, whereas $\Sigma 5$, $\Sigma 7$, and $\Sigma 17b$ occur in the experimental oxide scale. For similar phase boundaries between magnetite and hematite, their orientation relationship corresponds to the matching planes and directions $\{111\}_{Mn} \parallel \{0001\}_{Hm}$ and $\{110\}_{Mn} \parallel \{110\}_{Hm}$.
4. A relatively weak θ fiber, including a strong $\{001\}\langle 100 \rangle$ cube and a slightly strong $\{100\}\langle 210 \rangle$ texture components, develops in the magnetite of both the industrial and experimental oxide scales. The difference in the industrial oxide scale is the absence of the $\{001\}\langle 110 \rangle$ rotated cube component, due partly to shifting from $\{113\}\langle 110 \rangle$ and $\{111\}\langle 110 \rangle$ to $\{112\}\langle 110 \rangle$ texture components

ACKNOWLEDGMENTS

We are grateful to Dr. Daijun Yang at Shougang Research Institute of Technology, China, for the provision of the steel samples. Special thanks are given to Dr. Azdiar Gazder and Dr. Mitchell Nancarrow for their support and sharing enormous experiences on sample preparation and EBSD. The authors acknowledge the use of facilities within the UOW Electron Microscopy Centre. The authors wish to gratefully acknowledge the

help of Dr. Madeleine Strong Cincotta in the final language editing of this paper.

REFERENCES

1. T. Brune, D. Senk, R. Walpot, and B. Steenken: *Metall. Mater. Trans. B*, 2015, vol. 46B, pp. 1400–08.
2. M. Kiviö, L. Holappa, and T. Iung: *Metall. Mater. Trans. B*, 2010, vol. 41B, pp. 1194–1204.
3. F. Ma, G. Wen, P. Tang, G. Xu, F. Mei, and W. Wang: *Metall. Mater. Trans. B*, 2011, vol. 42B, pp. 81–86.
4. J. Hu, L.X. Du, J.J. Wang, and Q.Y. Sun: *Mater. Des.*, 2014, vol. 53, pp. 332–37.
5. T. Jia, Z. Liu, H. Hu, and G. Wang: *ISIJ Int.*, 2011, vol. 51, pp. 1468–73.
6. X. Yu, Z. Jiang, J. Zhao, D. Wei, C. Zhou, and Q. Huang: *Corros. Sci.*, 2014, vol. 85, pp. 115–25.
7. M. Krzyzanowski, J.H. Beynon, and C.M. Sellars: *Metall. Mater. Trans. B*, 2000, vol. 31B, pp. 1483–90.
8. Z. Jiang, X. Yu, J. Zhao, C. Zhou, Q. Huang, G. Luo, and K. Linghu: *Adv. Mater. Res.*, 2014, vol. 1017, pp. 435–40.
9. H.R. Le and M.P.F. Sutcliffe: *Metall. Mater. Trans. B*, 2004, vol. 35B, pp. 919–28.
10. X. Yu, Z. Jiang, J. Zhao, D. Wei, J. Zhou, C. Zhou, and Q. Huang: *Surf. Coat. Technol.*, 2015, vol. 272, pp. 39–49.
11. X. Yu, Z. Jiang, J. Zhao, D. Wei, C. Zhou, and Q. Huang: *Wear*, 2015, vols. 332–333, pp. 1286–92.
12. R.Y. Chen and W.Y.D. Yuen: *Oxid. Met.*, 2003, vol. 59, pp. 433–68.
13. M. Krzyzanowski, J.H. Beynon, and D.C. Farrugia: *Oxide Scale Behavior in High Temperature Metal Processing*, Wiley, Weinheim, 2010.
14. X.L. Yu, Z.Y. Jiang, X.D. Wang, D.B. Wei, and Q. Yang: *Adv. Mater. Res.*, 2012, vols. 415–417, pp. 853–58.
15. S.S. Mohapatra, J.M. Jha, S.V. Ravikumar, A. Singh, C. Bhattacharya, S.K. Pal, and S. Chakraborty: *Exp. Heat Transfer*, 2015, vol. 28, pp. 156–73.
16. R.Y. Chen and W.Y.D. Yuen: *Oxid. Met.*, 2001, vol. 56, pp. 89–118.
17. J. Miao, T.M. Pollock, and J.W. Jones: *Acta Mater.*, 2012, vol. 60, pp. 2840–54.
18. K.S. Chan: *Metall. Mater. Trans. A*, 2015, vol. 46A, pp. 2491–2505.
19. H. Abuluwefa, R.I.L. Guthrie, J.H. Root, and F. Ajersch: *Metall. Mater. Trans. B*, 1996, vol. 27B, pp. 993–97.
20. N. Birks, G.H. Meier, and F.S. Pettit: *Introduction to the High Temperature Oxidation of Metals*, 2nd ed., Cambridge University Press, New York, 2006, pp. 83–86.
21. DJ Young: *High Temperature Oxidation and Corrosion of Metals*, Elsevier, New York, 2008, pp. 37–42.
22. S. Hayashi, K. Mizumoto, S. Yoneda, Y. Kondo, H. Tanei, and S. Ukai: *Oxid. Met.*, 2014, vol. 81, pp. 357–71.
23. B. Gleeson, S.M.M. Hadavi, and D.J. Young: *Mater. High Temp.*, 2000, vol. 17, pp. 311–19.
24. S.I. Wright, M.M. Nowell, R. de Kloe, P. Camus, and T. Rampton: *Ultramicroscopy*, 2015, vol. 148, pp. 132–45.
25. A.A. Gazder, A.A. Saleh, M.J. Nancarrow, D.R. Mitchell, and E.V. Pereloma: *Steel Res. Int.*, 2015, vol. 86 (9999), pp. 1–11.
26. O. Engler and V. Randle: *Introduction to Texture Analysis: Macrotexture, Microtexture, and Orientation Mapping*, CRC press, Boca Raton, 2010, pp. 147–69.
27. Y. Tomota, S. Daikuhara, S. Nagayama, M. Sugawara, N. Ozawa, Y. Adachi, S. Harjo, and S. Hattori: *Metall. Mater. Trans. A*, 2014, vol. 45A, pp. 6103–17.
28. C. Juricic, H. Pinto, D. Cardinali, M. Klaus, C. Genzel, and A.R. Pyzalla: *Oxid. Met.*, 2010, vol. 73, pp. 15–41.
29. S. Liu, H. Wu, X. Li, H. Jiang, and D. Tang: *J. Iron. Steel Res. Int.*, 2014, vol. 21, pp. 215–21.
30. S. Biroasca, D. Dingley, and R.L. Higginson: *J. Microsc.*, 2004, vol. 213, pp. 235–40.
31. R.L. Higginson, B. Roebuck, and E.J. Palmiere: *Scripta Mater.*, 2002, vol. 47, pp. 337–42.

32. B.K. Kim and J.A. Szpunar: Orientation imaging microscopy in research on high temperature oxidation, in *Electron Backscatter Diffraction in Materials Science*, A.J. Schwartz, ed., Springer, New York, 2009, pp. 361–93.
33. L. Suárez, P. Rodríguez-Calvillo, Y. Houbaert, N.F. Garza-Montes-de-Oca, and R. Colás: *Oxid. Met.*, 2011, vol. 75, pp. 281–95.
34. M. Zhang and G. Shao: *Mater. Sci. Eng. A*, 2007, vols. 452–3, pp. 189–93.
35. X. Yu, Z. Jiang, and Q. Yang: *Adv. Mater. Res.*, 2011, vol. 145, pp. 111–16.
36. X. Yu, Z. Jiang, J. Zhao, D. Wei, C. Zhou, and Q. Huang: *Corros. Sci.*, 2015, vol. 90, pp. 140–52.
37. J.J.L. Mulders, R.T.J.P. Geurts, P.H.F. Trompenaars, and E.G.T. Bosch: *Low energy ion milling or deposition*, 2014, U.S. Patent Application 14/243,583.
38. M. Afshar and S. Zaeferrer: *Mater. Charact.*, 2015, vol. 101, pp. 130–35.
39. H.-J. Bunge: *Texture Analysis in Materials Science: Mathematical Methods*, Butterworth & Co., Berlin, 1982, pp. 3–41.
40. H. Okada, T. Fukagawa, H. Ishihara, A. Okamoto, M. Azuma, and Y. Matsuda: *ISIJ Int.*, 1995, vol. 35, pp. 886–91.
41. M. Graf and R. Kawalla: *Metall. Ital.*, 2014, vol. 2, pp. 43–49.
42. A.A. Gazder, V.Q. Vu, A.A. Saleh, P.E. Markovsky, O.M. Ivasishin, C.H. Davies, and E.V. Pereloma: *J. Alloys Compd.*, 2014, vol. 585, pp. 245–59.
43. X. Zhang, K. Matsuura, and M. Ohno: *Micron*, 2014, vol. 59, pp. 28–32.
44. H.E. Evans, H.Y. Li, and P. Bowen: *Scripta Mater.*, 2013, vol. 69, pp. 179–82.
45. J.A. Nychka, C. Pullen, M.Y. He, and D.R. Clarke: *Acta Mater.*, 2004, vol. 52, pp. 1097–1105.
46. H.E. Evans: *Int. Mater. Rev.*, 1995, vol. 40, pp. 1–40.
47. G.C. Wood and J. Stringer: *J. Phys. IV*, 1993, vol. 3, pp. 65–74.
48. M. Schütze: *Protective Oxide Scales and Their Breakdown*, Institute of Corrosion and Wiley, Chichester, 1997.
49. B.M. Morrow, R.J. McCabe, E.K. Cerreta, and C.N. Tomé: *Metall. Mater. Trans. A*, 2014, vol. 45, pp. 36–40.
50. J.O. Liu, S. Somnath, and W.P. King: *Sensor Actuators A-Phys.*, 2013, vol. 201, pp. 141–47.
51. F. Yang, X. Zhao, and P. Xiao: *Oxid. Met.*, 2014, vol. 81, pp. 331–43.
52. J. Robertson and M.I. Manning: *Mater. Sci. Technol.*, 1990, vol. 6, pp. 81–92.
53. V. Randle: *The Measurement of Grain Boundary Geometry*, IOP Publishing, Bristol and Philadelphia, 1993, pp. 33–56.
54. S. Kobayashi, A. Kamata, and T. Watanabe: *Acta Mater.*, 2015, vol. 91, pp. 70–82.
55. E.M. Lehockey, A.M. Brennenstuhl, and I. Thompson: *Corros. Sci.*, 2004, vol. 46, pp. 2383–2404.
56. J.H. Kim, B.K. Kim, D.I. Kim, P.P. Choi, D. Raabe, and K.W. Yi: *Corros. Sci.*, 2015, vol. 96, pp. 52–66.
57. J.Y. Kang, B. Bacroix, H. Réglé, K.H. Oh, and H.C. Lee: *Acta Mater.*, 2007, vol. 55, pp. 4935–46.
58. A.S. Azar, L.E. Svensson, and B. Nyhus: *Int. J. Fatigue*, 2015, vol. 77, pp. 95–104.
59. M. Shimada, H. Kokawa, Z.J. Wang, Y.S. Sato, and I. Karibe: *Acta Mater.*, 2002, vol. 50, pp. 2331–41.
60. S. Tsurekawa, S. Nakamichi, and T. Watanabe: *Acta Mater.*, 2006, vol. 54, pp. 3617–26.
61. M.A. Arafin and J.A. Szpunar: *Corros. Sci.*, 2009, vol. 51, pp. 119–28.
62. R. Pokharel, J. Lind, A.K. Kanjarla, R.A. Lebensohn, S.F. Li, P. Kenesei, R.M. Suter, and A.D. Rollett: *Annu. Rev. Condens. Matter Phys.*, 2014, vol. 5, pp. 317–46.